

# Engineering the non-Hermitian SSH model with skin effects in Rydberg atom arrays

J. N. Bai,<sup>1</sup> F. Yang,<sup>2,3</sup> D. Yan,<sup>4,\*</sup> Weibin Li,<sup>5</sup> and X. Q. Shao<sup>1,6,†</sup>

<sup>1</sup>*Center for Quantum Science and School of Physics, Northeast Normal University, Changchun 130024, China*

<sup>2</sup>*School of Physics and Zhejiang Key Laboratory of Micro-nano Quantum Chips and Quantum Control, Zhejiang University, Hangzhou 310027, China*

<sup>3</sup>*Niels Bohr International Academy, Niels Bohr Institute, University of Copenhagen, DK-2100 Copenhagen, Denmark*

<sup>4</sup>*College of Physics and Electronic Engineering, Hainan Normal University, Haikou 571158, China*

<sup>5</sup>*School of Physics and Astronomy, and Centre for the Mathematics and Theoretical Physics of Quantum Non-equilibrium Systems, The University of Nottingham, Nottingham NG7 2RD, United Kingdom*

<sup>6</sup>*Institute of Quantum Science and Technology, Yanbian University, Yanji 133002, China*

(Dated: January 29, 2026)

We propose and systematically analyze a practical scheme for implementing a one-dimensional non-Hermitian Su-Schrieffer-Heeger model using individually addressable Rydberg atom arrays. Our setup consists of an atomic chain with three-atom unit cells, in which a synthetic gauge field is generated by applying multi-color laser fields. By engineering fast dissipative channels for one auxiliary atom in each unit cell, the adiabatic elimination effectively gives rise to a non-Hermitian skin effect. We examine how fluctuations in the experimental parameters influence both the skin effect and the topological invariant under open and periodic boundary conditions in real space and find that both features remain highly robust. This work establishes a versatile, controllable, and programmable open-system quantum simulator with neutral atoms, providing a clear route for exploring rich non-Hermitian topological phenomena.

## I. INTRODUCTION

Rydberg atoms are neutral atoms excited to high-lying electronic states characterized by large principal quantum numbers, exhibiting enhanced properties such as strong long-range interactions, large polarizabilities, and long lifetimes [1–4]. Arrays of Rydberg atoms have become a powerful platform for quantum simulation and computation due to their highly tunable interactions mediated by dipole-dipole or van der Waals (vdW) forces [5–30]. This tunability enables the realization of diverse quantum spin models [19, 31–35] and provides a versatile testbed for studying quantum entanglement [36–43], many-body dynamics [44–48], and non-thermal phenomena such as quantum scars [36, 39, 49–57], as well as a wide range of non-equilibrium quantum behaviors [58]. Beyond spin dynamics, Rydberg systems also play a crucial role in exploring topological phases and quantum states [59–64]. Their precisely controllable interactions enable the realization of not only symmetry-protected topological (SPT) states but also stable states with intrinsic topological order (including those potentially hosting non-Abelian anyons) [65, 66]. These strongly topologically protected states, with enhanced robustness, have attracted considerable attention in the field of fault-tolerant quantum computation. Meanwhile, the phenomenon of controlling the dynamics of Rydberg atoms through engineered dissipation has attracted increasing interest in recent years [67–71], with continuous improvements in achieving the regime of the fastest relaxation rates [72]. Moreover, the high level of control over individual atoms offers promising opportunities for quantum optimization [73, 74] and the implementation of quantum algorithms [75, 76].

Non-Hermitian (NH) systems, characterized by mechanisms such as gain and loss or non-reciprocal hopping, exhibit rich spectral and topological features absent in Hermitian settings [77–85]. Under certain symmetry constraints, such as parity-time ( $\mathcal{PT}$ ) symmetry [86, 87], the spectra can remain entirely real, while beyond this regime, exotic phenomena such as half-integer winding numbers, exceptional rings [88–91], and the NH skin effect (NHSE) emerge [92–94]. The NHSE causes eigenstate accumulation near the system boundaries, thereby breaking the conventional bulk-boundary correspondence and motivating generalized theoretical frameworks, including non-Bloch band theory and biorthogonal polarization descriptions [79, 95]. In recent years, dissipation-engineered non-reciprocal transport has emerged as a powerful approach for achieving directional signal control in synthetic quantum systems. Such dissipative mechanisms can generate robust and tunable nonreciprocity, opening new possibilities for realizing chiral dynamics and topology-related phenomena [96, 97]. Recently, synthetic dimensions based on microwave-coupled Rydberg states have enabled the precise control of tunneling amplitudes and on-site potentials via microwave power and detuning. By engineering alternating coupling strengths, such systems can effectively emulate the Su-Schrieffer-Heeger (SSH) model, exhibiting symmetry-protected edge states and interaction-induced effects within a single atomic platform [98–101]. These developments have opened new avenues for investigating topological and NH phenomena in Rydberg atom platforms [87, 102–106]. Although synthetic dimensions offer a novel approach to topological physics, they are inherently limited by the number of accessible internal states and the site-dependent properties. In contrast, the Rydberg atom array platform offers scalable system sizes, identical lattice sites, and flexible geometric control, allowing for the direct implementation of complex non-reciprocal couplings and spatially resolved detection of the NHSE.

\* [yand@hainnu.edu.cn](mailto:yand@hainnu.edu.cn)

† [xqshao@nenu.edu.cn](mailto:xqshao@nenu.edu.cn)

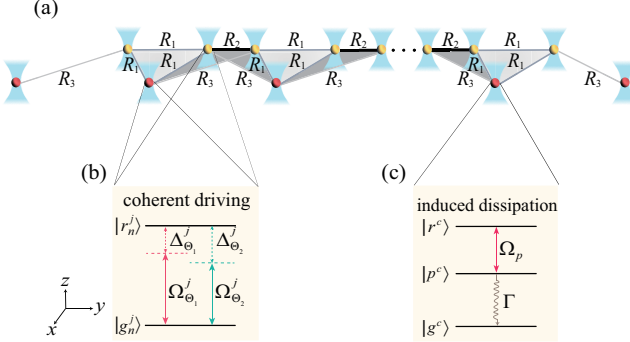


FIG. 1. (a) The schematic of a chain structure consisting of  $N$  three-atom unit cells. Each unit cell contains two data atoms (yellow) and one auxiliary atom (red), with the distances between atoms inside the unit cell labeled as  $R_1 = 6 \mu\text{m}$  and the adjacent unit cells denoted by  $R_2 = 3.46 \mu\text{m}$  and  $R_3 = 8.29 \mu\text{m}$ . (b) The laser driving process acting on both the data and auxiliary atoms, where neighboring atoms share the same laser, and each atom is driven by two distinct lasers. (c) A fast dissipative channel is constructed by introducing an intermediate state of the auxiliary atoms.

In this work, we engineer a synthetic gauge field in a Rydberg atom array using a photon-assisted excitation-exchange scheme. By dressing individually addressable atoms with multi-color laser fields [20, 107–109], we control spin-exchange interactions and utilize the adiabatic elimination of auxiliary atoms to induce non-reciprocal hopping. The remainder of this paper is organized as follows. In Sec. II, we introduce a system with a three-atom unit cell and analyze the effective dynamics of both the original and effective Hamiltonians in the single-excitation subspace, with particular emphasis on the intra-cell and inter-cell processes. In Sec. III, by adiabatically eliminating the auxiliary atoms through fast dissipative channels, we engineer non-reciprocal couplings for both intra- and inter-cell processes. In Sec. IV, we construct and implement a non-reciprocal SSH model with intra-cell and inter-cell couplings for an arbitrary number  $N$  of atoms under open boundary conditions (OBC). In Sec. V, we examine two primary noise sources: (i) phase disorder induced by fluctuations of the synthetic gauge flux, and (ii) positional disorder arising from the thermal motion of trapped atoms. The robustness of the system against these noise sources is characterized by the behavior of the skin-effect order parameter and topological invariant. In Sec. VI, we generalize the setup to a non-reciprocal SSH model under periodic boundary conditions (PBC). Finally, Sec. VII summarizes and concludes the study.

## II. THREE-ATOM UNIT-CELL CHAIN MODEL

We consider a Rydberg-atom array composed of  $N$  unit cells. Each unit cell hosts three individually addressable  $^{87}\text{Rb}$  atoms arranged at the vertices of an equilateral triangle with a side length  $R_1$ , as illustrated in Fig. 1(a). The

$j$ -th atom in the  $n$ -th cell is driven by two laser fields (a two-color drive) characterized by Rabi frequencies  $\Omega_\Theta^j = |\Omega_\Theta^j| e^{i\varphi_\Theta^j}$  and detunings  $\Delta_\Theta^j$  [see Fig. 1(b)], which couple the ground state  $|g_n^j\rangle = |5S_{1/2}, F = 2, m_F = 1\rangle$  to the Rydberg state  $|r_n^j\rangle = |70S_{1/2}, m_J = 1/2\rangle$ . The index  $\Theta$  runs over the set  $\{\Theta \mid \Theta = \text{I, II, III}\}$  of available lasers, and for a given atom, two of them, labeled  $\{\Theta_1, \Theta_2\} \subseteq \{\Theta\}$ , are applied simultaneously. The phase  $\varphi_\Theta^j$  specifies the optical phase of the laser addressing the  $j$ -th atom. In the interaction picture, the system Hamiltonian takes the form

$$H_I = \sum_{n=1}^N \left[ \sum_{j=a,b,c} \left( \frac{\Omega_{\Theta_1}^j}{2} e^{i\Delta_{\Theta_1}^j t} + \frac{\Omega_{\Theta_2}^j}{2} e^{i\Delta_{\Theta_2}^j t} \right) |r_n^j\rangle \langle g_n^j| + \text{H.c.} \right. \\ \left. - \sum_{j \neq k} \frac{C_6}{R^{jk}} |r_n^j r_n^k\rangle \langle r_n^j r_n^k| \right], \quad (1)$$

where  $C_6 \approx -863 \text{ GHz } \mu\text{m}^6$  is the van der Waals dispersion coefficient of the Rydberg state [110] and  $R^{jk}$  denotes the distance between the two interacting atoms. Throughout the article,  $a$  and  $b$  label the data atoms, while  $c$  denotes the auxiliary atom.

In the large-detuning regime  $|\Omega_\Theta^j| \ll |\Delta_\Theta^j|$ , an effective hopping amplitude  $J^{jk} = |J_{\Theta[jk]}^{jk}| e^{i\phi_{\Theta[jk]}^{jk}}$  corresponds to directed effective Rydberg-mediated transitions between atoms  $j$  and  $k$  [20] reads

$$|J_{\Theta[jk]}^{jk}| = \left| \frac{\Omega_{\Theta[jk]}^{j*} \Omega_{\Theta[jk]}^k V^{jk}}{4\Delta_{\Theta[jk]} (\Delta_{\Theta[jk]} + V^{jk})} \right|,$$

where  $V^{jk} = -C_6/R^{jk}^6$  defines the vdW interaction. Owing to the independent phase control of all dressing laser fields, a synthetic magnetic flux can be precisely threaded through a triangular plaquette formed by three atoms. The effective gauge flux enclosed by this closed loop is  $\Phi = (\varphi_I^a - \varphi_I^b) + (\varphi_{II}^b - \varphi_{II}^c) + (\varphi_{III}^c - \varphi_{III}^a)$ , where  $\varphi_{\Theta[jk]}^j$  and  $\varphi_{\Theta[jk]}^k$  are the phases imprinted by the same laser beam  $\Theta[jk]$  that mediates the dipolar interaction between the sites  $j$  and  $k$  (with  $\Theta^{[ab]} = \text{I}$ ,  $\Theta^{[bc]} = \text{II}$ , and  $\Theta^{[ca]} = \text{III}$ ). The resulting phase difference  $\phi_{\Theta[jk]}^{jk} = \varphi_{\Theta[jk]}^j - \varphi_{\Theta[jk]}^k$  enters the effective Hamiltonian as a Peierls phase factor. When both atoms are controlled by lasers of the same color, the energy mismatch  $\delta\Delta = |\Delta_{\Theta_1}^j - \Delta_{\Theta_2}^j|$  disappears. Consequently, the Rydberg excitation hopping channel between the two atoms can be established via monochromatic (single-frequency) laser dressing. Conversely, if lasers of different frequencies are applied to different atoms, a significant detuning mismatch occurs. When  $|\delta\Delta| \gg |J_{\Theta[jk]}^{jk}|$ , no Rydberg excitation hopping channel forms between them. A natural concern is that crosstalk inevitably arises between lasers of different colors. However, when the frequency difference between the two lasers is sufficiently large, this crosstalk becomes negligible. When  $\delta\Delta \simeq 0.1 \Omega_\Theta^j$ , the excitation dynamics become highly disordered, signaling the onset of a coherence collapse. In contrast,

when  $\delta\Delta \simeq 2\Omega_\Theta^j$ , regular and high-fidelity oscillatory dynamics appear. To obtain a net flux  $\Phi = \pm\pi/2$ , we simply choose  $\varphi_{\text{III}}^c = \pi/2$  while setting all other relevant laser-field phases to zero. This choice leads to Peierls phases  $\phi_{\text{III}}^{ca} = \pi/2$  and  $\phi_I^{ba} = \phi_{\text{II}}^{cb} = 0$ . Under these conditions, the excitation circulates unidirectionally around the triangular lattice plaquette (clockwise for  $+\pi/2$  and counterclockwise for  $-\pi/2$ ), thereby generating the characteristic chiral current associated with this flux-line configuration [111].

Since the Rydberg interaction is distance-dependent, couplings among all atoms should be included. However, as the interaction strength decays rapidly with increasing separation, it is sufficient to keep interactions within a finite range. To justify this approximation, as illustrated in Fig. 2(a), we consider a six-atom model that represents a local segment of the atomic array. This segment spans from the  $c$  atom in the  $(n-1)$ -th unit cell to the  $a$  and  $c$  atoms in the  $(n+1)$ -th unit cell, with  $n \in [2, N-1]$ , thereby forming three consecutively arranged auxiliary and data atoms. Given that the number of excitations is conserved and at most one atom can be promoted to the Rydberg state, we use second-order perturbation theory to derive the effective Hamiltonian for this system as

$$\begin{aligned} H_{\text{eff}} = & \mu_{n-1}^c \sigma_{n-1,c}^+ \sigma_{n-1,c}^- + \sum_{j=a,b,c} \mu_n^j \sigma_{n,j}^+ \sigma_{n,j}^- \\ & + \sum_{j=a,c} \mu_{n+1}^j \sigma_{n+1,j}^+ \sigma_{n+1,j}^- + J^{ab} \sigma_{n,a}^+ \sigma_{n,b}^- \\ & + J^{bc} \sigma_{n,b}^+ \sigma_{n,c}^- + iJ^{ca} (\sigma_{n,c}^+ \sigma_{n,a}^- + \sigma_{n+1,c}^+ \sigma_{n+1,a}^-) \\ & + J^{\text{inter}} \sigma_{n,b}^+ \sigma_{n+1,a}^- + h_1 \sigma_{n,b}^+ \sigma_{n+1,c}^- \\ & + ih_1 (\sigma_{n-1,c}^+ \sigma_{n,a}^- + \sigma_{n,c}^+ \sigma_{n+1,a}^-) + \text{H.c.}, \end{aligned} \quad (2)$$

where

$$\mu_n^j = \frac{|\Omega_{\Theta_1}^j|^2}{4\Delta_{\Theta_1}^j} + \frac{|\Omega_{\Theta_2}^j|^2}{4\Delta_{\Theta_2}^j} - \sum_{j \neq k} \left( \frac{|\Omega_{\Theta_1}^k|^2}{4\Delta_{\Theta_1}^k + V^{jk}} + \frac{|\Omega_{\Theta_2}^k|^2}{4\Delta_{\Theta_2}^k + V^{jk}} \right).$$

$J^{\text{inter}}$  and  $h_1$ ,  $h_2$  denote the inter-cell couplings and the interactions between the auxiliary atom and its nearest neighbor in the adjacent unit cell, respectively. In Fig. 2(b), we present the site-resolved population dynamics obtained from the time evolution governed by Eqs. (1) and (2). The two descriptions show excellent quantitative agreement for the populations on each lattice site, demonstrating that, in subsequent numerical simulations, interaction terms beyond a distance  $R > R_3$  can be safely neglected.

### III. NON-RECIPROCAL COUPLING BETWEEN ATOMS

#### A. Induced Dissipation of the Rydberg state

Given the long lifetime and weak spontaneous emission rate  $\gamma^c$  of the Rydberg state, constructing a non-Hermitian (NH) channel by directly adiabatically eliminating the auxiliary atom is unfeasible. To address this, we engineer a rapid relaxation process that transfers the auxiliary atom in the first unit cell

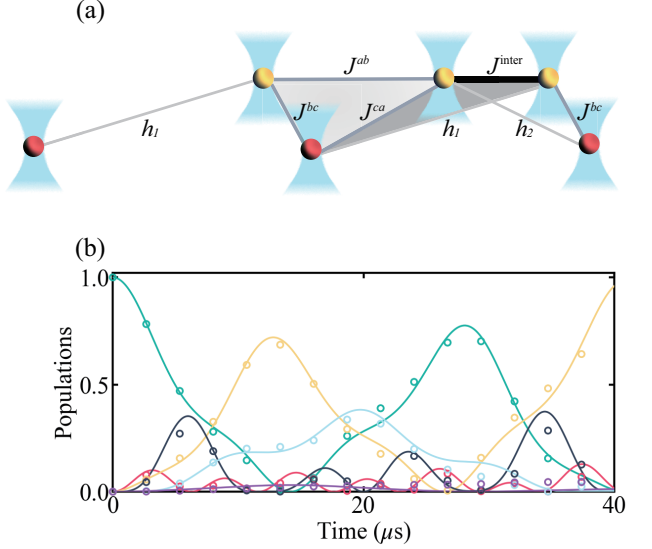


FIG. 2. (a) Illustration of the six-atom model. (b) Populations of the  $\sigma_{n-1,c}^+ \sigma_{n-1,c}^-$  (purple),  $\sigma_{n,a}^+ \sigma_{n,a}^-$  (green),  $\sigma_{n,b}^+ \sigma_{n,b}^-$  (red),  $\sigma_{n,c}^+ \sigma_{n,c}^-$  (yellow),  $\sigma_{n+1,a}^+ \sigma_{n+1,a}^-$  (black) and  $\sigma_{n+1,c}^+ \sigma_{n+1,c}^-$  (blue) governed by the equation of Eqs. (1) (hollow circle) and (2) (solid line), respectively. The detunings are  $(\Delta_I, \Delta_{\text{II}}, \Delta_{\text{III}}) = 2\pi \times (51.3, 59.8, 68.4)$  MHz with Rabi frequencies  $(\Omega_I, \Omega_{\text{II}}, \Omega_{\text{III}}) = 2\pi \times (4.3, 4.65, 5)$  MHz. Other parameters are taken as the same as Fig. 1.

from the Rydberg state  $|r^c\rangle$  to the target ground state  $|g^c\rangle$  via a short-lived intermediate state  $|p^c\rangle$ , as shown in Fig. 1(c), respectively. The dynamics of the subsystem are governed by two competing processes: coherent Rabi oscillations between the Rydberg and intermediate states driven at frequency  $\Omega_p$ , and incoherent spontaneous emission from the intermediate state to the ground state at a rate  $\Gamma$ . The optimization of the relaxation rate requires balancing these processes.

The Liouvillian superoperator  $\mathcal{L}$  of this three-level model can be expressed as

$$\begin{aligned} \mathcal{L} = & -i(H_{\text{rp}} \otimes \mathcal{I} - \mathcal{I} \otimes H_{\text{rp}}^T) + L_{\text{gp}} \otimes L_{\text{gp}}^* \\ & - \frac{1}{2}(L_{\text{gp}}^\dagger L_{\text{gp}} \otimes \mathcal{I} + \mathcal{I} \otimes L_{\text{gp}}^T L_{\text{gp}}^*), \end{aligned} \quad (3)$$

where  $H_{\text{rp}} = \Omega_p/2|p^c\rangle\langle r^c| + \text{H.c.}$ ,  $\mathcal{I}$  is the identity operator, and  $L_{\text{gp}} = \sqrt{\Gamma}|g^c\rangle\langle p^c|$ . The superscripts  $T$  and  $*$  denote the transpose and complex conjugation, respectively. The time evolution of the system is given by

$$\rho(t) = e^{\mathcal{L}t} \rho_{\text{in}} = \rho_{\text{ss}} + \sum_{i=1}^8 a_i e^{\lambda_i t} \mathbb{R}_i, \quad (4)$$

where  $\rho_{\text{ss}}$  is the unique steady state,  $\{\lambda_i\}$  are the complex eigenvalues of  $\mathcal{L}$ , and  $a_i = \text{Tr}[\mathbb{L}_i \rho_{\text{in}}]$  represents the projection of the initial state  $\rho_{\text{in}}$  onto the  $i$ -th right eigenmatrix  $\mathbb{R}_i$  (associated with the left eigenmatrix  $\mathbb{L}_i$ ). The relaxation timescale of the system is determined by the Liouvillian gap  $g$ , which is defined as the magnitude of the nonzero eigenvalue

with the smallest absolute real part. Using the basis states  $|g^c\rangle \equiv (1\ 0\ 0)^T$ ,  $|p^c\rangle \equiv (0\ 1\ 0)^T$ , and  $|r^c\rangle \equiv (0\ 0\ 1)^T$ , and assuming the initial state lies within the subspace  $\{|r^c\rangle, |p^c\rangle\}$ , the spectral gap is derived as

$$g = \text{Re} \left[ \frac{1}{2} (\Gamma - \kappa) \right], \quad (5)$$

where  $\kappa = \sqrt{\Gamma^2 - 4\Omega_p^2}$ .

The behavior of the spectral gap depends critically on the ratio of  $\Omega_p$  to  $\Gamma$ . In the weak driving regime ( $\Omega_p < \Gamma/2$ ),  $\kappa$  is real and positive, yielding a gap of  $g = (\Gamma - \kappa)/2$ . Standard Rydberg experiments typically operate in this regime to facilitate the adiabatic elimination of the intermediate state, resulting in an effective relaxation rate of  $\Omega_p^2/\Gamma$  [70, 71]. Although significantly faster than the natural decay of Rydberg states, this rate is inherently limited by the validity condition of the adiabatic approximation ( $\Omega_p \ll \Gamma$ ) and is insufficient for the auxiliary atom elimination required here. To overcome this limitation, we explore the strong driving regime ( $\Omega_p \geq \Gamma/2$ ). In this limit,  $\kappa$  becomes purely imaginary, resulting in a gap of  $g = \Gamma/2$ . Physically, the strong Rabi drive saturates the effective spontaneous emission of the Rydberg state at half the decay rate of the intermediate  $p$ -state. This enhancement allows the spectral gap of the NH band structure to reach its global maximum at the Liouvillian exceptional point [72].

## B. Adiabatic elimination creates non-reciprocal coupling

Taking into account the spontaneous decay of the data atoms at rates  $\gamma^a$  and  $\gamma^b$ , the system dynamics is governed by a Markovian master equation,

$$\dot{\rho} = -i[H'_{\text{eff}}, \rho] + 2L_{\text{gr}}^a \rho L_{\text{gr}}^{a\dagger} + L_{\text{gr}}^b \rho L_{\text{gr}}^{b\dagger} + 3L_{\text{gr}}^c \rho L_{\text{gr}}^{c\dagger}, \quad (6)$$

where the NH effective Hamiltonian is defined as

$$H'_{\text{eff}} = H_{\text{eff}} - \frac{i}{2} \left( 2L_{\text{gr}}^{a\dagger} L_{\text{gr}}^a + L_{\text{gr}}^{b\dagger} L_{\text{gr}}^b + 3L_{\text{gr}}^{c\dagger} L_{\text{gr}}^c \right), \quad (7)$$

with jump operators  $L_{\text{gr}}^a = \sqrt{\gamma^a} |g^a\rangle \langle r^a|$ ,  $L_{\text{gr}}^b = \sqrt{\gamma^b} |g^b\rangle \langle r^b|$  and  $L_{\text{gr}}^c = \sqrt{\Gamma/2} |g^c\rangle \langle r^c|$ . Here, we have neglected the spontaneous decay rate  $\gamma^c$  of the auxiliary atom since  $\gamma^c \ll \Gamma/2$ . Moreover, the Stark-shift terms appearing in Eq. (7) merely induce on-site energy offsets and do not affect the off-diagonal couplings; they, therefore, have no influence on the system dynamics of interest and can be safely neglected in the following analysis.

We now use  $u_x^y$  to denote the probability amplitude of atom  $x$  in the  $y$ -th unit cell being in the Rydberg state. In the Hamiltonian framework of Eq. (7), we restrict the dynamics to the single-excitation subspace, and the time evolution of the probability amplitudes  $u_x^y$  is then obtained by solving the corresponding Schrödinger equation

$$\dot{u}_{n-1}^c = -\frac{\Gamma}{2} u_{n-1}^c + h_1 u_n^a, \quad (8a)$$

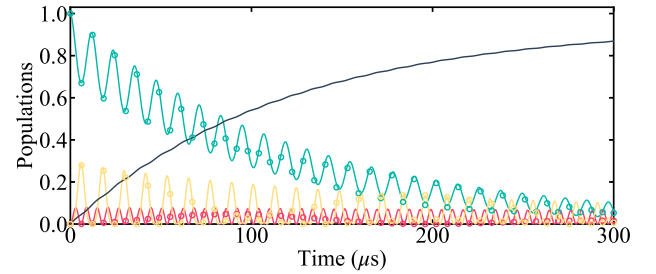


FIG. 3. Populations of the  $\sigma_{n,a}^+ \sigma_{n,a}^-$  (green),  $\sigma_{n,b}^+ \sigma_{n,b}^-$  (red),  $\sigma_{n+1,a}^+ \sigma_{n+1,a}^-$  (yellow), and  $\sigma_{n,j}^+ \sigma_{n,j}^-$  (black) governed by the Eq. (6) (solid line) and  $\sigma_{2n-1}^+ \sigma_{2n-1}^-$  (green),  $\sigma_{2n}^+ \sigma_{2n}^-$  (red),  $\sigma_{2n+1}^+ \sigma_{2n+1}^-$  (yellow) governed by the Eq. (10) (hollow circle), respectively. Other parameters are taken as the same as Figs. 1 and 2.

$$\dot{u}_n^a = -\gamma^a u_n^a - h_1 u_{n-1}^c - iJ^{ab} u_n^b - J^{ca} u_n^c, \quad (8b)$$

$$\dot{u}_n^b = -\gamma^b u_n^b - iJ^{ab} u_n^a - iJ^{bc} u_n^c - iJ^{\text{inter}} u_{n+1}^a - i h_2 u_{n+1}^c, \quad (8c)$$

$$\dot{u}_n^c = -\frac{\Gamma}{2} u_n^c + J^{ca} u_n^a - iJ^{bc} u_n^b + h_1 u_{n+1}^a. \quad (8d)$$

$$\dot{u}_{n+1}^a = -\gamma^a u_{n+1}^a - iJ^{\text{inter}} u_n^b - h_1 u_n^c - J^{ca} u_{n+1}^c. \quad (8e)$$

$$\dot{u}_{n+1}^c = -\frac{\Gamma}{2} u_{n+1}^c - i h_2 u_n^b + J^{ca} u_{n+1}^a. \quad (8f)$$

In the regime  $\Gamma/2 \gg \{\gamma^a, \gamma^b, J^{jk}\}$ , the rapidly decaying auxiliary atoms can be eliminated adiabatically. Through the mechanism, we enforce  $\dot{u}_{n-1}^c = \dot{u}_n^c = \dot{u}_{n+1}^c \approx 0$  and obtain

$$u_{n-1}^c = \frac{2}{\Gamma} h_1 u_n^a, \quad (9a)$$

$$u_n^c = \frac{2}{\Gamma} \left( J^{ca} u_n^a - iJ^{bc} u_n^b + h_1 u_{n+1}^a \right), \quad (9b)$$

$$u_{n+1}^c = \frac{2}{\Gamma} \left( -i h_2 u_n^b + J^{ca} u_{n+1}^a \right). \quad (9c)$$

Substituting Eq. (9) into Eq. (8) produces the effective dynamics

$$\dot{u}_n^a = - \left[ \gamma^a + \frac{2(J^{ca^2} + h_1^2)}{\Gamma} \right] u_n^a - i(J^{ab} - J_1) u_n^b, \quad (10a)$$

$$\begin{aligned} \dot{u}_n^b = & - \left[ \gamma^b + \frac{2(J^{bc^2} + h_2^2)}{\Gamma} \right] u_n^b - i(J^{ab} + J_1) u_n^a \\ & - i(J^{\text{inter}} + J_2) u_{n+1}^a, \end{aligned} \quad (10b)$$

$$\dot{u}_{n+1}^a = -\left[\gamma^a + \frac{2(J^{ca^2} + h_1^2)}{\Gamma}\right]u_{n+1}^a - i(J^{\text{inter}} - J_2)u_n^b, \quad (10c)$$

where  $J_1 \equiv 2J^{bc}J^{ca}/\Gamma$  and  $J_2 \equiv 2(J^{bc}h_1 + J^{ca}h_2)/\Gamma$ .

At room temperature (300 K), the lifetimes are  $\tau^{a,b} = 1/\gamma^{a(b)} = 104 \mu\text{s}$  for the Rydberg states  $|r^{a,b}\rangle$  and  $\tau = 1/\Gamma = 0.118 \mu\text{s}$  for the short-lived intermediate state  $|p^c\rangle = |6P_{3/2}, F = 3, m_F = 3\rangle$  [112, 113]. As shown in Fig. 3, the dynamical evolution obtained from Eq. (6) is in excellent agreement with that derived from the adiabatically eliminated model Eq. (10). This confirms the validity and effectiveness of the adiabatic elimination of the auxiliary atoms induced by engineered dissipation under the considered parameter regime. In addition, with  $\gamma^a + 2(J^{ca^2} + h_1^2)/\Gamma \approx \gamma^b + 2(J^{bc^2} + h_2^2)/\Gamma$ , the diagonally dissipative term acts as a global isotropic decay proportional to the identity matrix. Although this term sets the overall lifetime of the system, it does not affect the relative amplitudes or the topological structure of the eigenstates and can therefore be gauged away by post-selecting the experimental realizations where the excitation survives [87]. Finally, we obtain the following NH Hamiltonian

$$H_{\text{NH}} = J_L \sigma_{2n-1}^+ \sigma_{2n}^- + J_R \sigma_{2n}^+ \sigma_{2n-1}^- + G_L \sigma_{2n}^+ \sigma_{2n+1}^- + G_R \sigma_{2n+1}^+ \sigma_{2n}^-, \quad (11)$$

where  $J_L = J^{ab} + J_1$ ,  $J_R = J^{ab} - J_1$ ,  $G_L = J^{\text{inter}} - J_2$ , and  $G_R = J^{\text{inter}} + J_2$ . Unlike standard  $\mathcal{PT}$ -symmetric models that rely on balanced gain and loss on-site, Eq. (11) represents the NH SSH model with non-reciprocal hopping both within and between unit cells. Although these parameters can, in principle, be tuned by adjusting the lattice geometry, in our scheme large variations in the interatomic spacing would invalidate the conditions required for adiabatic elimination and perturbation theory. In the following discussion, we therefore assume  $G_L G_R > J_L J_R$ , such that the system is in a nontrivial topological phase.

#### IV. NON-HERMITIAN SSH MODEL UNDER OPEN BOUNDARY CONDITIONS

Under OBC, we extend the six-atom system to a Rydberg atom array comprising  $N = 20$  unit cells, thus obtaining the Hamiltonian of the NH SSH model for  $L = 40$  atoms,

$$H_{\text{OBC}} = \sum_{n=1}^{L/2} \left( J_L \sigma_{2n-1}^+ \sigma_{2n}^- + J_R \sigma_{2n}^+ \sigma_{2n-1}^- \right) + \sum_{n=1}^{L/2-1} \left( G_L \sigma_{2n}^+ \sigma_{2n+1}^- + G_R \sigma_{2n+1}^+ \sigma_{2n}^- \right). \quad (12)$$

The spectral properties of the NH system are investigated by numerically solving the eigenvalue equation  $H_{\text{OBC}}|\psi_n\rangle = E_n|\psi_n\rangle$ , where  $|\psi_n\rangle$  represents the  $n$ -th eigenstate. Due to the NH nature of the Hamiltonian, the energy eigenvalues  $E_n$  are complex-valued and can be decomposed as  $E_n = \epsilon_n - i\zeta_n/2$ . Here,  $\epsilon_n = \text{Re}(E_n)$  corresponds to the frequency shift of the

mode, while  $\zeta_n = -2\text{Im}(E_n)$  characterizes the effective decay rate induced by the dissipative channels. In Figs. 4(a1) and 4(a2), we plot the real and imaginary parts of  $E_n$ . The distribution of  $\text{Re}(E_n)$  shows a clear band gap, indicating the insulating nature of the bulk. Meanwhile, because the imaginary part  $\text{Im}(E_n)$  is approximately zero and can therefore be neglected, the system is in an unbroken  $\mathcal{PT}$ -symmetric phase. To understand the topological properties and the bulk-boundary correspondence of the non-reciprocal SSH model under OBC, we employ a similarity transformation  $\tilde{H}_{\text{OBC}} = S H_{\text{OBC}} S^{-1} = \tilde{H}_{\text{OBC}}^\dagger$ , where the similarity transformation matrix  $S$  is chosen to be diagonal. We set the first element as  $s_1 = 1$ , while the last two diagonal elements are given by  $s_{2N-1} = (l_1 l_2)^{N-1}$ ,  $s_{2N} = (l_1 l_2)^{N-1} l_1$ , with the scaling factors  $l_1 = \sqrt{J_L/J_R}$ ,  $l_2 = \sqrt{G_L/G_R}$ . Consequently, the matrix  $S$  takes the explicit form

$$S = \text{diag} \left[ 1, l_1, l_1 l_2, l_1^2 l_2, \dots, (l_1 l_2)^{N-1}, (l_1 l_2)^{N-1} l_1 \right]. \quad (13)$$

Since  $\tilde{H}_{\text{OBC}}$  is a Hermitian Hamiltonian, its eigenstates  $|\tilde{\psi}\rangle$  correspond to extended Bloch waves with uniform amplitude on the lattice, i.e.,  $|\tilde{\psi}(x)| \sim 1$ . The eigenstates  $|\psi\rangle$  are related to  $|\tilde{\psi}\rangle$  through an inverse similarity transformation. As a result, the amplitude of the wavefunction in the  $n$ -th lattice is modulated by the inverse of the diagonal element of  $S$ ,

$$\psi_n \propto s_n^{-1} \tilde{\psi}_n \sim (l_1 l_2)^{-n/2} e^{ikn}. \quad (14)$$

If the hopping asymmetry is directional,  $s_n$  grows exponentially with the lattice index  $n$ . Consequently, the wavefunction  $\psi_n$  decays exponentially, leading to the localization of all bulk states at the boundary of the system. The normalized eigenstates obtained from Eq. (12) are localized at the boundaries of the system in Figs. 4(b1) and 4(b2), which is a hallmark of the NHSE.

## V. EFFECTS OF DISORDER ON THE NHSE

### A. Characterization Measures of NHSE

To quantify the spatial confinement of the eigenstates, we employ the inverse participation ratio (IPR), defined as  $\text{IPR} = \sum_{j=1}^L |\psi_{n,j}|^4 / (\langle \psi_n | \psi_n \rangle)^2$ . Physically, a vanishing  $\text{IPR} \sim 1/L$  corresponds to a delocalized state, whereas  $\text{IPR} \approx 1$  signifies strict localization. To further resolve the characteristic of directional asymmetry in the NHSE, the signed directional IPR (dIPR) is adopted by Refs. [114, 115]

$$\text{dIPR}(\psi_n) = \mathcal{P}(\psi_n) \text{IPR}. \quad (15)$$

Here, the polarization factor  $\mathcal{P}(\psi_n)$  determines the spatial bias of the wave function and is defined as

$$\mathcal{P}(\psi_n) = \text{sgn} \left[ \sum_{j=1}^L \left( j - \frac{L}{2} - \delta \right) |\psi_{n,j}| \right], \quad (16)$$

where  $\delta$  is a small symmetry-breaking constant. This factor assigns a positive (negative) sign to states located on the

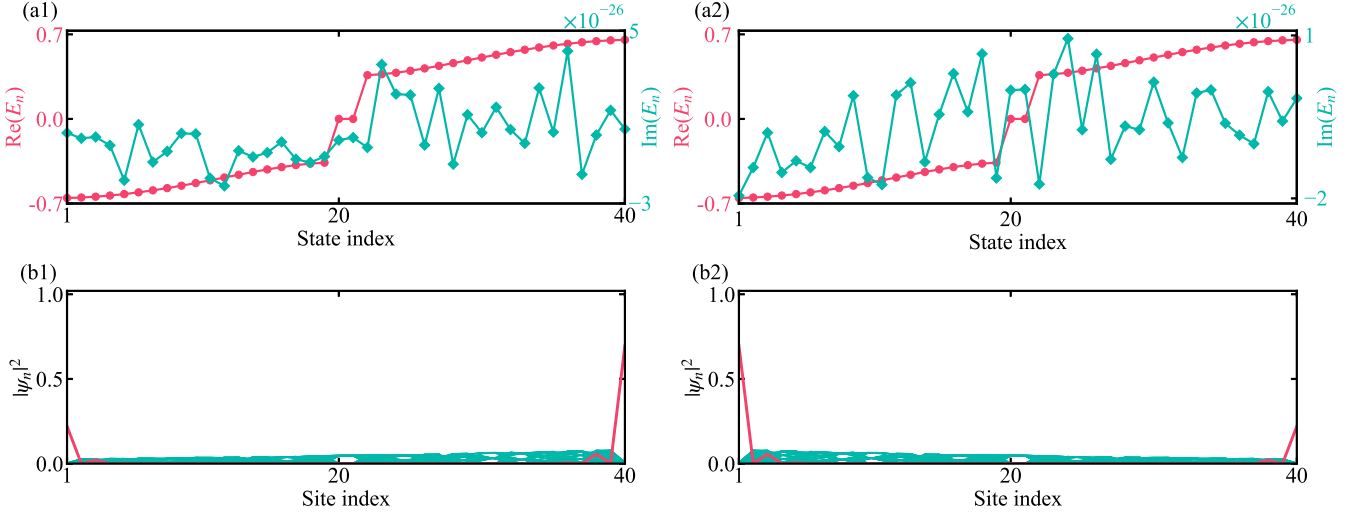


FIG. 4. (a1) and (a2) represent the complex energy spectra of Eq. (12) under different parameter regimes, corresponding to  $\phi_{ca} = \pi/2$  and  $-\pi/2$ , respectively. The red circles (left axis) denote the real part of the eigenvalues  $\text{Re}(E_n)$  and the green diamonds (right axis) represent the imaginary part  $\text{Im}(E_n)$ . (b1) and (b2) display the spatial probability distributions  $|\psi_n|^2$  of the eigenstates associated with the spectra in (a). The red line highlights the topologically protected edge states localized at the boundary, whereas the green lines depict the extended bulk states. Other parameters are taken as the same as Figs. 1 and 2.

right (left) boundary. The global localization behavior is then summarized by the directional mean IPR (dMIPR), which is obtained by averaging over all eigenstates

$$\text{dMIPR} = \frac{1}{L} \sum_{n=1}^L \text{dIPR}(\psi_n). \quad (17)$$

The topological robustness of the system in the presence of disorder is characterized by the winding number in real-space. This formulation is based on the biorthogonal basis of the NH effective Hamiltonian  $H_{\text{OBC}}$ . To ensure the proper algebraic properties of the projection operators, the left  $\{|nL\rangle\}$  and right  $\{|nR\rangle\}$  eigenvectors are rigorously normalized to satisfy the biorthonormality condition  $\langle mL|nR \rangle = \delta_{mn}$ . Using the chiral symmetry operator  $S_1 = \bigoplus_{j=1}^N \sigma_z$ , where  $\{S_1, H_{\text{OBC}}\} = 0$ , the flattened Hamiltonian  $Q = \mathbb{I} - 2P$  is constructed from the projector  $P = \sum_{n=1}^N |nR\rangle\langle nL|$  onto the subspace of occupied states. The real-space winding number  $\nu_s$  is then physically derived as the trace of the chiral displacement operator [116, 117]

$$\nu_s = \frac{1}{2N'} \text{Tr}'(S_1 Q [Q, X]), \quad (18)$$

where  $X$  is the coordinate operator and  $[Q, X]$  encodes the topological correlations between the unit cells. The trace  $\text{Tr}'$  is restricted to a bulk window  $N' = L - 2l_1$  to eliminate finite-size edge effects, where  $l_1$  represents the boundary cutoff length. Finally, to evaluate the stability of topological quantization against noise, the disorder-averaged winding number is calculated over an ensemble of  $N_s$  realizations [118, 119]:

$$\nu = \frac{1}{N_s} \sum_{s=1}^{N_s} \nu_s. \quad (19)$$

A value of  $1 - \nu \approx 0$  indicates that the topological quantization is robust against the level of noise introduced, whereas a significant deviation suggests a breakdown of the topological protection. Crucially, unlike momentum space invariants that strictly require translational symmetry, this real-space formulation is universally applicable. It remains a strictly well-defined and quantized topological invariant regardless of the boundary conditions, making it suitable for characterizing both the ideal periodic lattice and the disordered systems where translational invariance is explicitly broken.

## B. Phase Disorder

Although the synthetic magnetic flux is, in principle, fixed by the lattice geometry and the prescribed laser-phase configuration, unavoidable experimental imperfections introduce small random perturbations to the enclosed flux. These fluctuations primarily originate from slow relative phase drifts between the interfering laser beams and weak spatial inhomogeneities in the detuning, both of which modify the complex tunneling amplitudes. To model such experimentally relevant effects, we incorporate phase disorder into the non-reciprocal hopping by introducing independent random phase offsets  $\delta\phi$  into all hopping channels associated with the III laser (other phase fluctuations in the system can be equivalently accounted for by a gauge transformation and absorbed into the phase of the III laser), leading to the effective Hamiltonian,

$$H_{\delta\phi} = \sum_{n=1}^{L/2} \left( J'_L \sigma_{2n-1}^+ \sigma_{2n}^- + J'_R \sigma_{2n}^+ \sigma_{2n-1}^- \right)$$

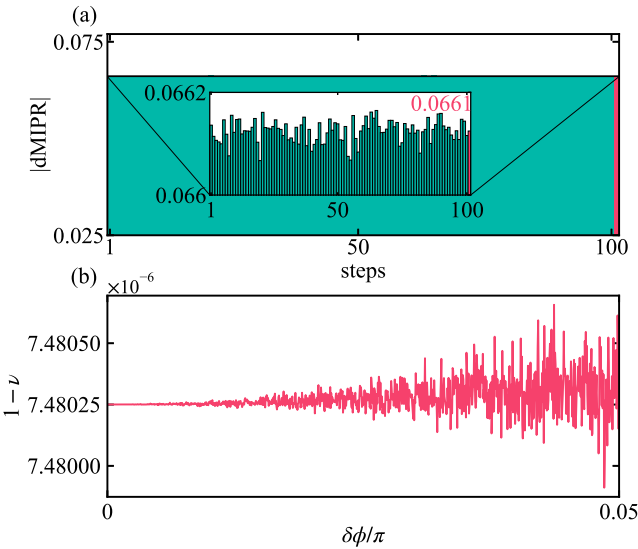


FIG. 5. (a) After introducing Mean-distributed phase noise to the  $\phi_{ca}$  phase of each link in a 20 unit-cell chain, the  $|dMIPR|$  is calculated according to Eq. (20) for  $N_s = 100$  independent realizations of random  $\delta\phi$ . The green bars represent the value for each individual disordered realization, while the red bar indicates the average value. (b) The deviation of the winding number  $1 - v$  as a function of uniform disorder strength. Other parameters are taken as the same as Figs. 1 and 2.

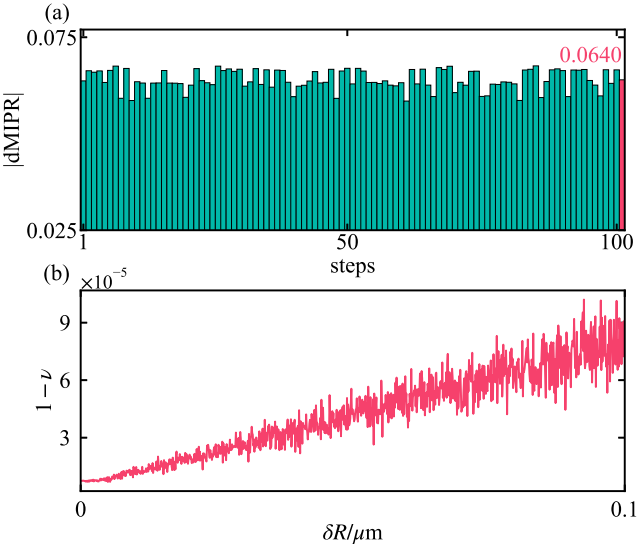


FIG. 6. (a) The  $|dMIPR|$  calculated for  $N_s = 100$  independent realizations of positional disorder using the effective Hamiltonian in Eq. (21). The red bar indicates the averaged value. (b) The deviation of the winding number  $1 - v$  as a function of the positional disorder strength. Other parameters are taken as the same as Figs. 1 and 2.

$$+ \sum_{n=1}^{L/2-1} \left( G'_L \sigma_{2n}^+ \sigma_{2n+1}^- + G'_R \sigma_{2n+1}^+ \sigma_{2n}^- \right), \quad (20)$$

where

$$J^{jk'} = \left| \frac{\Omega_{\Theta[jk]}^{j*} \Omega_{\Theta[jk]}^k V^{jk}}{4\Delta_{\Theta[jk]} (\Delta_{\Theta[jk]} + V^{jk})} \right| e^{i(\phi_{\Theta[jk]}^{jk} + \delta\phi)}$$

with

$$J'_L = J^{ab} - i \frac{2J^{bc} J^{ca'}}{\Gamma}, \quad G'_L = J^{\text{inter}} + i \frac{2(J^{bc} h'_1 + J^{ca'} h'_2)}{\Gamma}$$

$$J'_R = J^{ab} + i \frac{2J^{bc} J^{ca'}}{\Gamma}, \quad G'_R = J^{\text{inter}} - i \frac{2(J^{bc} h'_1 + J^{ca'} h'_2)}{\Gamma}.$$

In Fig. 5(a), phase disorder is implemented by assigning an independent random phase shift to each unit cell. Phase fluctuations are sampled from a uniform distribution,  $\delta\phi \sim \mathcal{U}(-\eta, \eta)$ , where  $\eta$  is chosen to be 10 % of the Peierls phase  $\pi/2$ . Since skin localization toward the left and right boundaries is symmetric in our system and differs only by an overall sign, we adopt the absolute value  $|dMIPR|$  as a unified measure to characterize the skin effect induced localization at either boundary. The resulting ensemble-averaged  $dMIPR$  remains robustly positive and far from  $1/L = 0.025$  ( $|dMIPR| \approx 0.0661$ ), demonstrating that the localization bias persists even under experimentally accessible unit-cell phase noise. In Fig. 5(b), we examine the topological invariant as a function of the disorder strength. As the strength of the disorder increases, the winding number of the real-space  $1 - v$  gradually deviates from zero due to finite-size effects, while  $v$  remains close to its quantized value, confirming the robustness of the topological phase against phase disorder.

### C. Position Disorder

In realistic experiments, atomic positions cannot be perfectly fixed because of the finite temperature and residual technical noise in optical tweezers. Each atom is confined in a tightly focused trap and is therefore described by a wave-packet with finite spatial width arising from zero-point motion and thermal fluctuations. The typical positional deviation ranges from  $0.01 \mu\text{m}$  to  $0.1 \mu\text{m}$ , depending specifically on the depth and temperature of the trap [57, 120–122]. Because the Rydberg interaction scales with the interatomic distance as  $V^{jk} \propto 1/R^{jk^6}$ , even sub-micrometer positional fluctuations can substantially alter interatomic distances and the corresponding effective interaction energies. To incorporate positional disorder, we replace the ideal interatomic distance  $R$  with  $R + \delta R$ , where  $\delta R$  is a random displacement, modifying the effective Hamiltonian as

$$H_{\delta R} = \sum_{n=1}^{L/2} \left( J''_L \sigma_{2n-1}^+ \sigma_{2n}^- + J''_R \sigma_{2n}^+ \sigma_{2n-1}^- \right) + \sum_{n=1}^{L/2-1} \left( G''_L \sigma_{2n}^+ \sigma_{2n+1}^- + G''_R \sigma_{2n+1}^+ \sigma_{2n}^- \right), \quad (21)$$

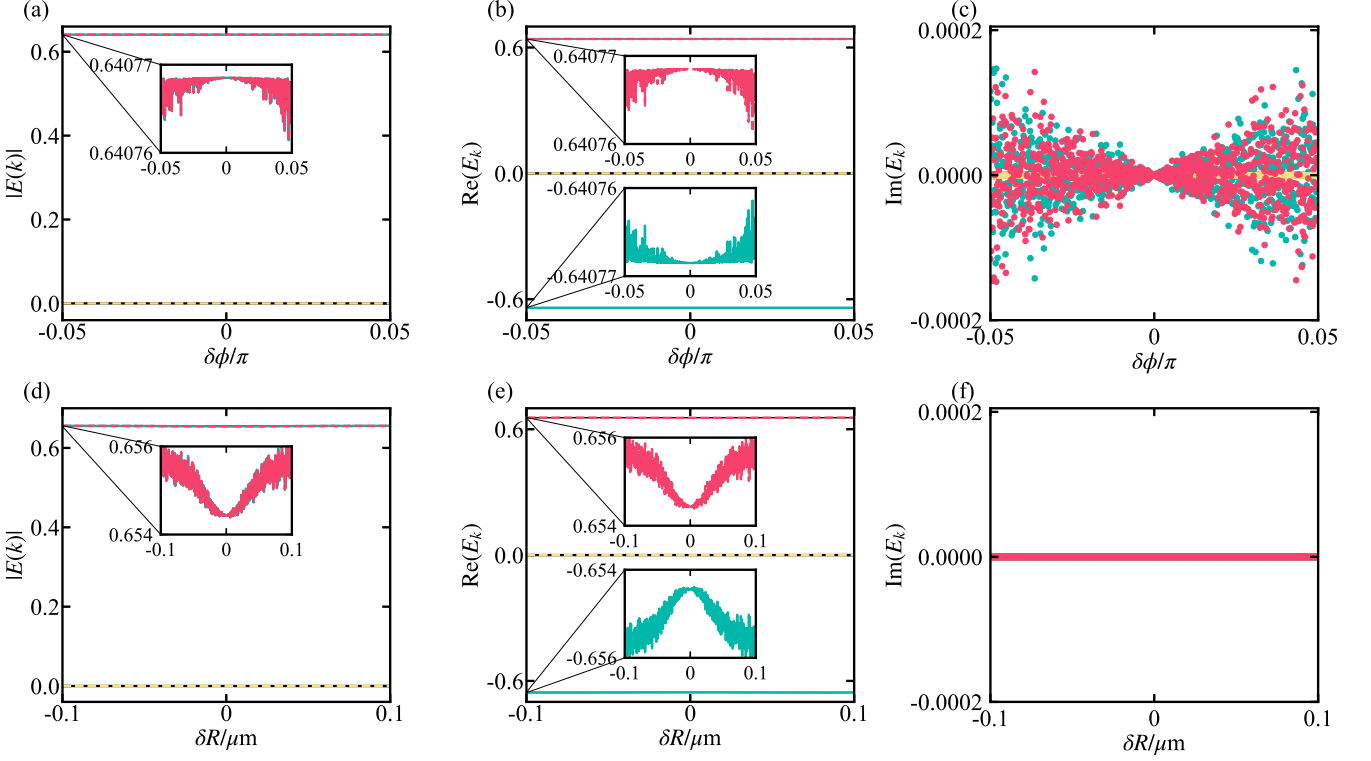


FIG. 7. Evolution of the complex eigenenergies of the NH SSH chain under random phase and position disorder. Panels (a–c) and (d–f) respectively depict the dependence of  $|E(k)|$ ,  $\text{Re}(E_k)$ , and  $\text{Im}(E_k)$  on the normalized phase fluctuation  $\delta\phi/\pi$  in Eq. (20) and position fluctuation  $\delta R/\mu\text{m}$  in Eq. (21). The trajectories corresponding to four representative eigenmodes with indices  $k = 1$  (green solid line), 20 (black solid line), 21 (yellow dashed line) and 40 (red dashed line) are shown for comparison. Other parameters are taken as the same as Figs. 1 and 2.

where

$$J^{jk''} = \left| \frac{\Omega_{\Theta[jk]}^{j*} \Omega_{\Theta[jk]}^k V^{jk''}}{4\Delta_{\Theta[jk]} (\Delta_{\Theta[jk]} + V^{jk''})} \right| e^{i\phi_{\Theta[jk]}^{jk}}$$

with  $V^{jk''} = -C_6/(R + \delta R)^6$  in

$$J_L'' = J^{ab''} + \frac{2J^{bc''} J^{ca''}}{\Gamma}, \quad J_R'' = J^{ab''} - \frac{2J^{bc''} J^{ca''}}{\Gamma},$$

$$G_L'' = J^{\text{inter}''} - \frac{2(J^{bc''} h_1'' + J^{ca''} h_2'')}{\Gamma},$$

$$G_R'' = J^{\text{inter}''} + \frac{2(J^{bc''} h_1'' + J^{ca''} h_2'')}{\Gamma}.$$

In Fig. 6(a), independent random perturbations are applied to all interatomic distances, and each perturbation is uniformly sampled from the interval  $\delta R \in [-0.1, 0.1] \mu\text{m}$ . The resulting ensemble-averaged localization measure remains robust, with  $|\text{dMIPR}| \approx 0.0639$ , indicating that moderate positional fluctuations do not suppress the non-reciprocal transport asymmetry. As shown in Fig. 6(b), the winding number of the real-space  $1 - v$  stays close to zero throughout the entire disorder range,

demonstrating that the chiral symmetry protected topological phase remains intact in the presence of realistic geometric imperfections.

We now examine the evolution of the complex eigen-spectrum under weak phase  $\delta\phi$  and position disorder  $\delta R$ . As shown in Fig. 7, both the spectral magnitude  $|E_k|$  and the real part  $\text{Re}(E_k)$  vary smoothly with the strength of disorder, while two nearly flat spectral branches exhibit only minimal deviations, indicating that the associated edge states are largely insensitive to applied perturbations. In Fig. 7(c), for phase disorder, the Hamiltonian  $H_{\delta\phi}$  becomes intrinsically complex due to explicit factors  $e^{\pm i(\pi/2 + \delta\phi)}$ , breaking the symmetry required for a purely real spectrum and leading to finite imaginary parts of the eigenvalues. In contrast, for Fig. 7(f),  $H_{\delta R}$  retains non-reciprocal couplings of real value, and the system remains in the  $\mathcal{PT}$ -symmetric phase within  $\delta R \leq 0.1 \mu\text{m}$ , ensuring a purely real spectrum. This result demonstrates that the topological edge states are robust against small geometric deformations and remain stable as long as the disorder strength does not drive the system across an exceptional point.

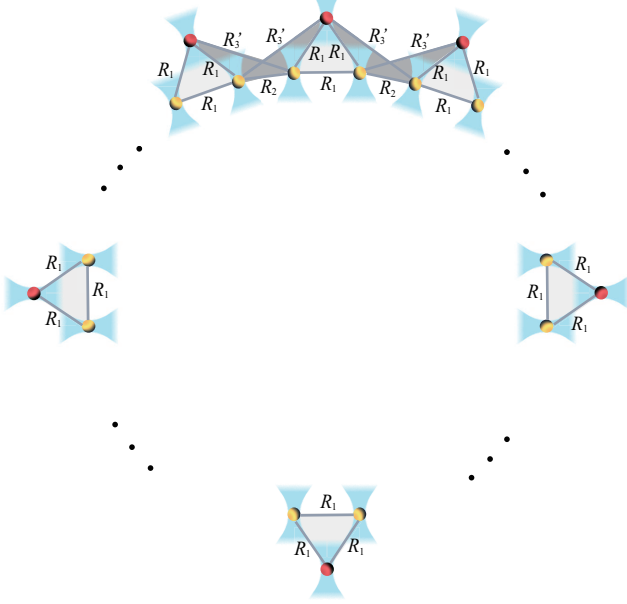


FIG. 8. The schematic of a chain structure consisting of  $N = 20$  three-atom unit cells arranged in a ring configuration to implement PBC.

## VI. GENERALIZATION TO PERIODIC-BOUNDARY NON-HERMITIAN SSH MODEL

To elucidate the bulk topological origin of the NHSE observed under OBC, we extend the system to PBC. In contrast to open chains, PBC eliminates the localization effects induced by the boundary and thus provides direct access to the intrinsic bulk topology of the system. Due to the presence of non-reciprocal hopping, the conventional bulk-boundary correspondence is generally invalid, making it essential to characterize the topology using real-space quantities.

As shown in Fig. 8, we construct a ring geometry consisting of 20 unit cells to implement PBC. Unlike the OBC configuration, no additional auxiliary atoms are required at the boundaries. Instead, those in the first and last unit cells jointly establish the inter-cell non-reciprocal hopping channel, thereby closing the chain into a ring. The spatial arrangement is chosen such that the relevant interatomic distances are preserved. By precisely matching the chord lengths with distances  $R_1$  and  $R_2$ , the effective coupling strengths remain consistent with those in the open-chain case, while a larger separation  $R'_3 \approx 8.61 \mu\text{m}$  suppresses unwanted cross-couplings  $R > R'_3$ . Under these conditions, the effective Hamiltonian with PBC is given by

$$H_{\text{PBC}} = \sum_{n=1}^{L/2} \left( J_L \sigma_{2n-1}^+ \sigma_{2n}^- + J_R \sigma_{2n}^+ \sigma_{2n-1}^- \right) + \sum_{n=1}^{L/2-1} \left( G_L \sigma_{2n}^+ \sigma_{2n+1}^- + G_R \sigma_{2n+1}^+ \sigma_{2n}^- \right) + G_L \sigma_L^+ \sigma_1^- + G_R \sigma_1^+ \sigma_L^- \quad (22)$$

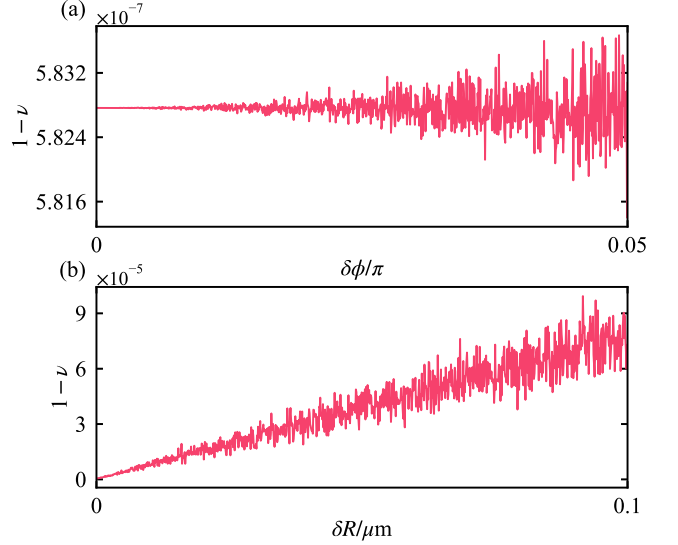


FIG. 9. The deviation  $1 - \nu$  as a function of the phase  $\delta\phi$  (a) and disorder strength  $\delta R$  (b) in Eq. (22). The results are averaged over  $N_s$  realizations. Other parameters are taken as the same as Figs. 1 and 2.

To characterize the bulk topology in real-space, we compute the deviation of the winding number of the real-space from its quantized value,  $1 - \nu$ , as a function of the strength of disorder. As shown in Figs. 9(a) and 9(b),  $1 - \nu$  remains close to zero throughout the range of considered disorder. Since  $\nu \approx 1$  corresponds to a nontrivial winding, this result demonstrates that the bulk topological phase is preserved under PBC despite the presence of realistic experimental disorder. The robustness of  $1 - \nu$  further implies that the non-reciprocal hopping channels retain their dominant chiral structure at the bulk scale. Consequently, the system maintains its nontrivial topological character, ensuring the persistence of the NHSE once the boundaries are reopened.

## VII. CONCLUSION

In summary, we propose a Rydberg atom array composed of unit cells with three atoms each. By introducing engineered dissipation, the auxiliary atoms can be adiabatically eliminated, leading to an effective model with non-reciprocal couplings both within and between the unit cells. We further investigate the influence of noise by analyzing the skin-effect order parameter and the topological invariant, and find that the non-Hermitian topological features remain robust over a broad range of noise strengths. Notably, our scheme is formulated directly in real space, in contrast to approaches based on synthetic dimensions. This feature enables a faithful implementation of both open and periodic boundary conditions in the SSH model, which is essential for the transparent characterization of non-Hermitian topology. Given the intrinsic interactions between Rydberg atoms and the high degree of controllability of dissipation and coupling in such systems, our approach provides a natural route toward programmable

and scalable realizations of non-Hermitian topological dynamics. An interesting direction for future work is to extend the present scheme to interacting topological chain models, where the combined effects of non-Hermiticity, topology, and many-body interactions can be explored systematically.

## ACKNOWLEDGMENTS

This work was supported by the National Natural Science Foundation (Grants No. 12174048 and 12564047). W.L.

acknowledges support from the EPSRC through Grant No. EP/W015641/1. F.Y. acknowledges the support from the Firuza Foundation Fellowship and helpful discussions with B. Yan and X. Wu.

## DATA AVAILABILITY

The data that support the findings of this article are openly available [123].

---

[1] T. F. Gallagher, *Rydberg Atoms*, Cambridge Monographs on Atomic, Molecular and Chemical Physics (Cambridge University Press, 1994).

[2] M. Saffman, T. G. Walker, and K. Mølmer, Quantum information with Rydberg atoms, *Rev. Mod. Phys.* **82**, 2313 (2010).

[3] M. Saffman, Quantum computing with atomic qubits and Rydberg interactions: progress and challenges, *Journal of Physics B: Atomic, Molecular and Optical Physics* **49**, 202001 (2016).

[4] X.-Q. Shao, S.-L. Su, L. Li, R. Nath, J.-H. Wu, and W. Li, Rydberg superatoms: An artificial quantum system for quantum information processing and quantum optics, *Applied Physics Reviews* **11**, 031320 (2024).

[5] D. Barredo, S. Ravets, H. Labuhn, L. Béguin, A. Vernier, F. Nogrette, T. Lahaye, and A. Browaeys, Demonstration of a strong Rydberg blockade in three-atom systems with anisotropic interactions, *Phys. Rev. Lett.* **112**, 183002 (2014).

[6] Z. Meir, O. Schwartz, E. Shahmoon, D. Oron, and R. Ozeri, Cooperative Lamb Shift in a mesoscopic atomic array, *Phys. Rev. Lett.* **113**, 193002 (2014).

[7] H. Schempp, G. Günter, S. Wüster, M. Weidemüller, and S. Whitlock, Correlated exciton transport in Rydberg-dressed-atom spin chains, *Phys. Rev. Lett.* **115**, 093002 (2015).

[8] H. Labuhn, D. Barredo, S. Ravets, S. De Léséleuc, T. Macrì, T. Lahaye, and A. Browaeys, Tunable two-dimensional arrays of single Rydberg atoms for realizing quantum Ising models, *Nature* **534**, 667 (2016).

[9] M. Endres, H. Bernien, A. Keesling, H. Levine, E. R. Anschuetz, A. Krajenbrink, C. Senko, V. Vuletic, M. Greiner, and M. D. Lukin, Atom-by-atom assembly of defect-free one-dimensional cold atom arrays, *Science* **354**, 1024 (2016).

[10] T. L. Nguyen, J. M. Raimond, C. Sayrin, R. Cortiñas, T. Cantat-Moltrecht, F. Assemat, I. Dotsenko, S. Gleyzes, S. Haroche, G. Roux, T. Jolicoeur, and M. Brune, Towards quantum simulation with circular Rydberg atoms, *Phys. Rev. X* **8**, 011032 (2018).

[11] S. Basak, Y. Chougale, and R. Nath, Periodically driven array of single Rydberg atoms, *Phys. Rev. Lett.* **120**, 123204 (2018).

[12] F. M. Gambetta, W. Li, F. Schmidt-Kaler, and I. Lesanovsky, Engineering nonbinary Rydberg interactions via phonons in an optical lattice, *Phys. Rev. Lett.* **124**, 043402 (2020).

[13] R. Menu and T. Roscilde, Anomalous diffusion and localization in a positionally disordered quantum spin array, *Phys. Rev. Lett.* **124**, 130604 (2020).

[14] C. Sheng, J. Hou, X. He, P. Xu, K. Wang, J. Zhuang, X. Li, M. Liu, J. Wang, and M. Zhan, Efficient preparation of two-dimensional defect-free atom arrays with near-fewest sorting atom moves, *Phys. Rev. Res.* **3**, 023008 (2021).

[15] F. Liu, Z.-C. Yang, P. Bienias, T. Iadecola, and A. V. Gorshkov, Localization and criticality in antiblockaded two-dimensional Rydberg atom arrays, *Phys. Rev. Lett.* **128**, 013603 (2022).

[16] S. Hollerith, K. Srakaew, D. Wei, A. Rubio-Abadal, D. Adler, P. Weckesser, A. Kruckenhauser, V. Walther, R. van Bijnen, J. Rui, C. Gross, I. Bloch, and J. Zeiher, Realizing distance-selective interactions in a Rydberg-dressed atom array, *Phys. Rev. Lett.* **128**, 113602 (2022).

[17] J. Ramette, J. Sinclair, Z. Vendeiro, A. Rudelis, M. Cetina, and V. Vuletić, Any-to-any connected cavity-mediated architecture for quantum computing with trapped ions or Rydberg arrays, *PRX Quantum* **3**, 010344 (2022).

[18] C. Dlaska, K. Ender, G. B. Mbeng, A. Kruckenhauser, W. Lechner, and R. van Bijnen, Quantum optimization via four-body Rydberg gates, *Phys. Rev. Lett.* **128**, 120503 (2022).

[19] P. Scholl, H. J. Williams, G. Bornet, F. Wallner, D. Barredo, L. Henriet, A. Signoles, C. Hainaut, T. Franz, S. Geier, A. Tebben, A. Salzinger, G. Zürn, T. Lahaye, M. Weidemüller, and A. Browaeys, Microwave engineering of programmable XXZ Hamiltonians in arrays of Rydberg atoms, *PRX Quantum* **3**, 020303 (2022).

[20] X. Wu, F. Yang, S. Yang, K. Mølmer, T. Pohl, M. K. Tey, and L. You, Manipulating synthetic gauge fluxes via multicolor dressing of Rydberg-atom arrays, *Phys. Rev. Res.* **4**, L032046 (2022).

[21] C. Nill, K. Brandner, B. Olmos, F. Carollo, and I. Lesanovsky, Many-body radiative decay in strongly interacting Rydberg ensembles, *Phys. Rev. Lett.* **129**, 243202 (2022).

[22] K. Srakaew, P. Weckesser, S. Hollerith, D. Wei, D. Adler, I. Bloch, and J. Zeiher, A subwavelength atomic array switched by a single Rydberg atom, *Nature Physics* **19**, 714 (2023).

[23] V. Bharti, S. Sugawa, M. Mizoguchi, M. Kunimi, Y. Zhang, S. de Léséleuc, T. Tomita, T. Franz, M. Weidemüller, and K. Ohmori, Picosecond-scale ultrafast many-body dynamics in an ultracold Rydberg-excited atomic Mott insulator, *Phys. Rev. Lett.* **131**, 123201 (2023).

[24] S. J. Evered, D. Bluvstein, M. Kalinowski, S. Ebadi, T. Manovitz, H. Zhou, S. H. Li, A. A. Geim, T. T. Wang, N. Maskara, *et al.*, High-fidelity parallel entangling gates on a neutral-atom quantum computer, *Nature* **622**, 268 (2023).

[25] S. Ma, G. Liu, P. Peng, B. Zhang, S. Jandura, J. Claes, A. P. Burgers, G. Pupillo, S. Puri, and J. D. Thompson, High-fidelity gates and mid-circuit erasure conversion in an atomic qubit, *Nature* **622**, 279 (2023).

[26] L. Zhao, M. D. K. Lee, M. M. Aliyu, and H. Loh, Floquet-tailored Rydberg interactions, *Nature Communications* **14**, 7128 (2023).

[27] N. Chepiga, Tunable quantum criticality in multicomponent Rydberg arrays, *Phys. Rev. Lett.* **132**, 076505 (2024).

[28] P. M. Ireland, D. M. Walker, and J. D. Pritchard, Interspecies Förster resonances for Rb-Cs Rydberg  $d$ -states for enhanced multi-qubit gate fidelities, *Phys. Rev. Res.* **6**, 013293 (2024).

[29] T. Zhang and Z. Cai, Quantum slush state in Rydberg atom arrays, *Phys. Rev. Lett.* **132**, 206503 (2024).

[30] N. U. Koyluoglu, N. Maskara, J. Feldmeier, and M. D. Lukin, Floquet engineering of interactions and entanglement in periodically driven Rydberg chains, *Phys. Rev. Lett.* **135**, 113603 (2025).

[31] C. Chen, G. Bornet, M. Bintz, G. Emperauger, L. Leclerc, V. S. Liu, P. Scholl, D. Barredo, J. Hauschild, S. Chatterjee, *et al.*, Continuous symmetry breaking in a two-dimensional Rydberg array, *Nature* **616**, 691 (2023).

[32] L.-M. Steinert, P. Osterholz, R. Eberhard, L. Festa, N. Lorenz, Z. Chen, A. Trautmann, and C. Gross, Spatially tunable spin interactions in neutral atom arrays, *Phys. Rev. Lett.* **130**, 243001 (2023).

[33] G. Bornet, G. Emperauger, C. Chen, B. Ye, M. Block, M. Bintz, J. A. Boyd, D. Barredo, T. Comparin, F. Mezzacapo, *et al.*, Scalable spin squeezing in a dipolar Rydberg atom array, *Nature* **621**, 728 (2023).

[34] K. Slagle, Y. Liu, D. Aasen, H. Pichler, R. S. K. Mong, X. Chen, M. Endres, and J. Alicea, Quantum spin liquids bootstrapped from Ising criticality in Rydberg arrays, *Phys. Rev. B* **106**, 115122 (2022).

[35] H. Sable, N. M. Myers, and V. W. Scarola, Toward quantum analog simulation of many-body supersymmetry with Rydberg atom arrays, *Phys. Rev. Lett.* **135**, 033401 (2025).

[36] A. Omran, H. Levine, A. Keesling, G. Semeghini, T. T. Wang, S. Ebadi, H. Bernien, A. S. Zibrov, H. Pichler, S. Choi, *et al.*, Generation and manipulation of Schrödinger cat states in Rydberg atom arrays, *Science* **365**, 570 (2019).

[37] T. M. Graham, M. Kwon, B. Grinkemeyer, Z. Marra, X. Jiang, M. T. Lichtman, Y. Sun, M. Ebert, and M. Saffman, Rydberg-mediated entanglement in a two-dimensional neutral atom qubit array, *Phys. Rev. Lett.* **123**, 230501 (2019).

[38] Z.-Y. Wei, D. Malz, A. González-Tudela, and J. I. Cirac, Generation of photonic matrix product states with Rydberg atomic arrays, *Phys. Rev. Res.* **3**, 023021 (2021).

[39] N. Maskara, A. A. Michailidis, W. W. Ho, D. Bluvstein, S. Choi, M. D. Lukin, and M. Serbyn, Discrete time-crystalline order enabled by quantum many-body scars: Entanglement steering via periodic driving, *Phys. Rev. Lett.* **127**, 090602 (2021).

[40] T. Graham, Y. Song, J. Scott, C. Poole, L. Phuttitarn, K. Jooya, P. Eichler, X. Jiang, A. Marra, B. Grinkemeyer, *et al.*, Multi-qubit entanglement and algorithms on a neutral-atom quantum computer, *Nature* **604**, 457 (2022).

[41] N. Schine, A. W. Young, W. J. Eckner, M. J. Martin, and A. M. Kaufman, Long-lived Bell states in an array of optical clock qubits, *Nature Physics* **18**, 1067 (2022).

[42] M. J. O'Rourke and G. K.-L. Chan, Entanglement in the quantum phases of an unfrustrated Rydberg atom array, *Nature Communications* **14**, 5397 (2023).

[43] P. L. Ocola, I. Dimitrova, B. Grinkemeyer, E. Guardado-Sánchez, T. Đorđević, P. Samutpraphoot, V. Vuletić, and M. D. Lukin, Control and entanglement of individual Rydberg atoms near a nanoscale device, *Phys. Rev. Lett.* **132**, 113601 (2024).

[44] H. Bernien, S. Schwartz, A. Keesling, H. Levine, A. Omran, H. Pichler, S. Choi, A. S. Zibrov, M. Endres, M. Greiner, *et al.*, Probing many-body dynamics on a 51-atom quantum simulator, *Nature* **551**, 579 (2017).

[45] Y. Wang, S. Shevate, T. M. Wintermantel, M. Morgado, G. Lochead, and S. Whitlock, Preparation of hundreds of microscopic atomic ensembles in optical tweezer arrays, *npj Quantum Information* **6**, 54 (2020).

[46] D. Bluvstein, A. Omran, H. Levine, A. Keesling, G. Semeghini, S. Ebadi, T. T. Wang, A. A. Michailidis, N. Maskara, W. W. Ho, *et al.*, Controlling quantum many-body dynamics in driven Rydberg atom arrays, *Science* **371**, 1355 (2021).

[47] S. Ebadi, T. T. Wang, H. Levine, A. Keesling, G. Semeghini, A. Omran, D. Bluvstein, R. Samajdar, H. Pichler, W. W. Ho, *et al.*, Quantum phases of matter on a 256-atom programmable quantum simulator, *Nature* **595**, 227 (2021).

[48] S. Ma, A. P. Burgers, G. Liu, J. Wilson, B. Zhang, and J. D. Thompson, Universal gate operations on nuclear spin qubits in an optical tweezer array of  $^{171}\text{Yb}$  atoms, *Phys. Rev. X* **12**, 021028 (2022).

[49] W. W. Ho, S. Choi, H. Pichler, and M. D. Lukin, Periodic orbits, entanglement, and quantum many-body scars in constrained models: Matrix product state approach, *Phys. Rev. Lett.* **122**, 040603 (2019).

[50] A. A. Michailidis, C. J. Turner, Z. Papić, D. A. Abanin, and M. Serbyn, Stabilizing two-dimensional quantum scars by deformation and synchronization, *Phys. Rev. Res.* **2**, 022065 (2020).

[51] C. J. Turner, J.-Y. Desaules, K. Bull, and Z. Papić, Correspondence principle for many-body scars in ultracold Rydberg atoms, *Phys. Rev. X* **11**, 021021 (2021).

[52] B. Windt and H. Pichler, Squeezing quantum many-body scars, *Phys. Rev. Lett.* **128**, 090606 (2022).

[53] R. Shen, F. Qin, J.-Y. Desaules, Z. Papić, and C. H. Lee, Enhanced many-body quantum scars from the non-Hermitian Fock skin effect, *Phys. Rev. Lett.* **133**, 216601 (2024).

[54] A. N. Ivanov and O. I. Motrunich, Volume-entangled exact scar states in the PXP and related models in any dimension, *Phys. Rev. Lett.* **134**, 050403 (2025).

[55] X. Liang, Z. Yue, Y.-X. Chao, Z.-X. Hua, Y. Lin, M. K. Tey, and L. You, Observation of anomalous information scrambling in a Rydberg atom array, *Phys. Rev. Lett.* **135**, 050201 (2025).

[56] J.-L. Ma, Z. Guo, Y. Gao, Z. Papić, and L. Ying, Liouvillian spectral transition in noisy quantum many-body scars, *Phys. Rev. Lett.* **135**, 180401 (2025).

[57] L. Zhao, P. R. Datla, W. Tian, M. M. Aliyu, and H. Loh, Observation of quantum thermalization restricted to Hilbert Space fragments and  $F_{2k}$  scars, *Phys. Rev. X* **15**, 011035 (2025).

[58] A. Deger, A. Daniel, Z. Papić, and J. K. Pachos, Persistent non-Gaussian correlations in out-of-equilibrium Rydberg atom arrays, *PRX Quantum* **4**, 040339 (2023).

[59] S. De Léséleuc, V. Lienhard, P. Scholl, D. Barredo, S. Weber, N. Lang, H. P. Büchler, T. Lahaye, and A. Browaeys, Observation of a symmetry-protected topological phase of interacting bosons with Rydberg atoms, *Science* **365**, 775 (2019).

[60] G. Semeghini, H. Levine, A. Keesling, S. Ebadi, T. T. Wang, D. Bluvstein, R. Verresen, H. Pichler, M. Kalinowski, R. Samajdar, *et al.*, Probing topological spin liquids on a programmable quantum simulator, *Science* **374**, 1242 (2021).

[61] P. S. Tarabunga, F. M. Surace, R. Andreoni, A. Angelone, and M. Dalmonte, Gauge-theoretic origin of Rydberg quantum spin liquids, *Phys. Rev. Lett.* **129**, 195301 (2022).

[62] R. Samajdar, D. G. Joshi, Y. Teng, and S. Sachdev, Emergent  $F_2$  gauge theories and topological excitations in Rydberg atom arrays, *Phys. Rev. Lett.* **130**, 043601 (2023).

[63] Z. Yan, Y.-C. Wang, R. Samajdar, S. Sachdev, and Z. Y. Meng, Emergent glassy behavior in a kagome Rydberg atom array, *Phys. Rev. Lett.* **130**, 206501 (2023).

[64] Z. Yue, Y.-F. Mao, X. Liang, Z.-X. Hua, P. Ge, Y.-X. Chao, K. Li, C. Jia, M. K. Tey, Y. Xu, and L. You, *Observation of average topological phase in disordered Rydberg atom array* (2025), [arXiv:2505.06286 \[cond-mat.quant-gas\]](https://arxiv.org/abs/2505.06286).

[65] N. M. Bauer, E. Kokkas, V. Ale, and G. Siopsis, Non-Abelian anyons with Rydberg atoms, *Phys. Rev. A* **107**, 062407 (2023).

[66] M. Kalinowski, N. Maskara, and M. D. Lukin, Non-Abelian floquet spin liquids in a digital Rydberg simulator, *Phys. Rev. X* **13**, 031008 (2023).

[67] X.-Q. Shao, Selective Rydberg pumping via strong dipole blockade, *Phys. Rev. A* **102**, 053118 (2020).

[68] X. Q. Shao, F. Liu, X. W. Xue, W. L. Mu, and W. Li, High-fidelity interconversion between Greenberger-Horne-Zeilinger and W states through Floquet-Lindblad engineering in Rydberg atom arrays, *Phys. Rev. Appl.* **20**, 014014 (2023).

[69] Y.-L. Zhou, X.-D. Yu, C.-W. Wu, X.-Q. Li, J. Zhang, W. Li, and P.-X. Chen, Accelerating relaxation through Liouvillian exceptional point, *Phys. Rev. Res.* **5**, 043036 (2023).

[70] B. Bégo, G. Cichelli, S. P. Singh, F. Bensch, V. Amico, F. Perciavalle, D. Rossini, L. Amico, and O. Morsch, Controlled dissipation for rydberg atom experiments, *Phys. Rev. A* **112**, 023312 (2025).

[71] T. Chen, C. Huang, J. P. Covey, and B. Gadway, Collective dissipation engineering of interacting rydberg atoms, *Phys. Rev. Lett.* **135**, 253402 (2025).

[72] F. Q. Guo, S.-L. Su, W. Li, and X. Q. Shao, *Scalable steady-state entanglement with Floquet-engineered stabilizer pumping in neutral atom arrays* (2025), [arXiv:2509.18379 \[quant-ph\]](https://arxiv.org/abs/2509.18379).

[73] S. Ebadi, A. Keesling, M. Cain, T. T. Wang, H. Levine, D. Bluvstein, G. Semeghini, A. Omran, J.-G. Liu, R. Samajdar, *et al.*, Quantum optimization of maximum independent set using Rydberg atom arrays, *Science* **376**, 1209 (2022).

[74] M. Lenthaler, C. Dlaska, K. Ender, and W. Lechner, Rydberg-blockade-based parity quantum optimization, *Phys. Rev. Lett.* **130**, 220601 (2023).

[75] M.-T. Nguyen, J.-G. Liu, J. Wurtz, M. D. Lukin, S.-T. Wang, and H. Pichler, Quantum optimization with arbitrary connectivity using Rydberg atom arrays, *PRX Quantum* **4**, 010316 (2023).

[76] A. Llenas and L. Lamata, Digital-analog quantum genetic algorithm using Rydberg-atom arrays, *Phys. Rev. A* **110**, 042603 (2024).

[77] F. K. Kunst, E. Edvardsson, J. C. Budich, and E. J. Bergholtz, Biorthogonal bulk-boundary correspondence in non-Hermitian systems, *Phys. Rev. Lett.* **121**, 026808 (2018).

[78] S. Yao and Z. Wang, Edge states and topological invariants of non-Hermitian systems, *Phys. Rev. Lett.* **121**, 086803 (2018).

[79] K. Yokomizo and S. Murakami, Non-bloch band theory of non-Hermitian systems, *Phys. Rev. Lett.* **123**, 066404 (2019).

[80] N. Okuma and M. Sato, Topological phase transition driven by infinitesimal instability: Majorana fermions in non-Hermitian spintronics, *Phys. Rev. Lett.* **123**, 097701 (2019).

[81] K. Kawabata, K. Shiozaki, M. Ueda, and M. Sato, Symmetry and topology in non-Hermitian physics, *Phys. Rev. X* **9**, 041015 (2019).

[82] Z. Yang, K. Zhang, C. Fang, and J. Hu, Non-Hermitian bulk-boundary correspondence and auxiliary generalized brillouin zone theory, *Phys. Rev. Lett.* **125**, 226402 (2020).

[83] E. J. Bergholtz, J. C. Budich, and F. K. Kunst, Exceptional topology of non-Hermitian systems, *Rev. Mod. Phys.* **93**, 015005 (2021).

[84] H.-G. Zirnstein, G. Rafael, and B. Rosenow, Bulk-boundary correspondence for non-Hermitian Hamiltonians via green functions, *Phys. Rev. Lett.* **126**, 216407 (2021).

[85] F. Schindler, K. Gu, B. Lian, and K. Kawabata, Hermitian bulk – non-Hermitian boundary correspondence, *PRX Quantum* **4**, 030315 (2023).

[86] C. M. Bender and S. Boettcher, Real spectra in non-Hermitian Hamiltonians having  $\mathcal{PT}$  symmetry, *Phys. Rev. Lett.* **80**, 5243 (1998).

[87] J. A. S. Lourenço, G. Higgins, C. Zhang, M. Hennrich, and T. Macrì, Non-Hermitian dynamics and  $\mathcal{PT}$ -symmetry breaking in interacting mesoscopic Rydberg platforms, *Phys. Rev. A* **106**, 023309 (2022).

[88] Y. Xu, S.-T. Wang, and L.-M. Duan, Weyl exceptional rings in a three-dimensional dissipative cold atomic gas, *Phys. Rev. Lett.* **118**, 045701 (2017).

[89] K. Kawabata, T. Bessho, and M. Sato, Classification of exceptional points and non-Hermitian topological semimetals, *Phys. Rev. Lett.* **123**, 066405 (2019).

[90] J.-J. Liu, Z.-W. Li, Z.-G. Chen, W. Tang, A. Chen, B. Liang, G. Ma, and J.-C. Cheng, Experimental realization of Weyl exceptional rings in a synthetic three-dimensional non-Hermitian phononic crystal, *Phys. Rev. Lett.* **129**, 084301 (2022).

[91] S. Bid and H. Schomerus, Uniform response theory of non-Hermitian systems: Non-Hermitian physics beyond the exceptional point, *Phys. Rev. Res.* **7**, 023062 (2025).

[92] N. Okuma, K. Kawabata, K. Shiozaki, and M. Sato, Topological origin of non-Hermitian skin effects, *Phys. Rev. Lett.* **124**, 086801 (2020).

[93] K. Kawabata, T. Numasawa, and S. Ryu, Entanglement phase transition induced by the non-Hermitian skin effect, *Phys. Rev. X* **13**, 021007 (2023).

[94] Q. Liang, D. Xie, Z. Dong, H. Li, H. Li, B. Gadway, W. Yi, and B. Yan, Dynamic signatures of non-Hermitian skin effect and topology in ultracold atoms, *Phys. Rev. Lett.* **129**, 070401 (2022).

[95] E. Edvardsson, F. K. Kunst, T. Yoshida, and E. J. Bergholtz, Phase transitions and generalized biorthogonal polarization in non-Hermitian systems, *Phys. Rev. Res.* **2**, 043046 (2020).

[96] A. Metelmann and A. A. Clerk, Nonreciprocal photon transmission and amplification via reservoir engineering, *Phys. Rev. X* **5**, 021025 (2015).

[97] X. Huang, C. Lu, C. Liang, H. Tao, and Y.-C. Liu, Loss-induced nonreciprocity, *Light: Science & Applications* **10**, 30 (2021).

[98] S. Kanungo, J. Whalen, Y. Lu, M. Yuan, S. Dasgupta, F. Dunning, K. Hazzard, and T. Killian, Realizing topological edge states with Rydberg-atom synthetic dimensions, *Nature communications* **13**, 972 (2022).

[99] Y. Lu, C. Wang, S. K. Kanungo, S. Yoshida, F. B. Dunning, and T. C. Killian, Wave-packet dynamics and long-range tunneling within the Su-Schrieffer-Heeger model using Rydberg-atom synthetic dimensions, *Phys. Rev. A* **109**, 032801 (2024).

[100] Y. Lu, C. Wang, S. K. Kanungo, F. B. Dunning, and T. C. Killian, Probing the topological phase transition in the Su-Schrieffer-Heeger Hamiltonian using Rydberg-atom synthetic dimensions, *Phys. Rev. A* **110**, 023318 (2024).

[101] M. Trautmann, I. Sodemann Villadiego, and J. Deiglmayr, Realization of topological thouless pumping in a synthetic Rydberg dimension, *Phys. Rev. A* **110**, L040601 (2024).

[102] A. Arias, G. Lochead, T. M. Wintermantel, S. Helmrich, and S. Whitlock, Realization of a Rydberg-dressed Ramsey interferometer and electrometer, *Phys. Rev. Lett.* **122**, 053601 (2019).

[103] Z. Gong, N. Yoshioka, N. Shibata, and R. Hamazaki, Universal error bound for constrained quantum dynamics, *Phys. Rev. Lett.* **124**, 210606 (2020).

[104] L. Li, C. H. Lee, and J. Gong, Topological switch for non-Hermitian skin effect in cold-atom systems with loss, *Phys. Rev. Lett.* **124**, 250402 (2020).

[105] R. Shen, T. Chen, M. M. Aliyu, F. Qin, Y. Zhong, H. Loh, and C. H. Lee, Proposal for observing Yang-Lee criticality in Rydberg atomic arrays, *Phys. Rev. Lett.* **131**, 080403 (2023).

[106] D. Roberts and A. A. Clerk, Exact solution of the infinite-range dissipative transverse-field Ising model, *Phys. Rev. Lett.* **131**, 190403 (2023).

[107] F. Yang, S. Yang, and L. You, Quantum transport of Rydberg excitons with synthetic spin-exchange interactions, *Phys. Rev. Lett.* **123**, 063001 (2019).

[108] F. Yang, Y.-C. Liu, and L. You, Atom-photon spin-exchange collisions mediated by Rydberg dressing, *Phys. Rev. Lett.* **125**, 143601 (2020).

[109] T. Manovitz, Y. Shapira, N. Akerman, A. Stern, and R. Ozeri, Quantum simulations with complex geometries and synthetic gauge fields in a trapped ion chain, *PRX Quantum* **1**, 020303 (2020).

[110] N. Šibalić, J. D. Pritchard, C. S. Adams, and K. J. Weatherill, ARC: An open-source library for calculating properties of alkali Rydberg atoms, *Computer Physics Communications* **220**, 319 (2017).

[111] X. X. Li, J. B. You, X. Q. Shao, and W. Li, Coherent ground-state transport of neutral atoms, *Phys. Rev. A* **105**, 032417 (2022).

[112] I. I. Beterov, I. I. Ryabtsev, D. B. Tretyakov, and V. M. Entin, Quasiclassical calculations of blackbody-radiation-induced depopulation rates and effective lifetimes of Rydberg  $nS$ ,  $nP$ , and  $nD$  alkali-metal atoms with  $n \leq 80$ , *Phys. Rev. A* **79**, 052504 (2009).

[113] X. X. Li, X. Q. Shao, and W. Li, Single temporal-pulse-modulated parameterized controlled-phase gate for Rydberg atoms, *Phys. Rev. Appl.* **18**, 044042 (2022).

[114] Q.-B. Zeng and R. Lü, Real spectra and phase transition of skin effect in nonreciprocal systems, *Phys. Rev. B* **105**, 245407 (2022).

[115] Y.-W.-Y. Li, X.-F. Nie, J. Cao, W.-X. Cui, and H.-F. Wang, Topological phases and non-Hermitian topology in tunable nonreciprocal cyclic three-mode optical systems, *Opt. Express* **32**, 13562 (2024).

[116] A. Kitaev, Anyons in an exactly solved model and beyond, *Annals of Physics* **321**, 2 (2006).

[117] F. Song, S. Yao, and Z. Wang, Non-Hermitian topological invariants in real space, *Phys. Rev. Lett.* **123**, 246801 (2019).

[118] I. Mondragon-Shem, T. L. Hughes, J. Song, and E. Prodan, Topological criticality in the chiral-symmetric AIII class at strong disorder, *Phys. Rev. Lett.* **113**, 046802 (2014).

[119] D.-W. Zhang, L.-Z. Tang, L.-J. Lang, H. Yan, and S.-L. Zhu, Non-Hermitian topological Anderson insulators, *Science China Physics, Mechanics & Astronomy* **63**, 267062 (2020).

[120] M. Marcuzzi, J. c. v. Minář, D. Barredo, S. de Léséleuc, H. Labuhn, T. Lahaye, A. Browaeys, E. Levi, and I. Lesanovsky, Facilitation dynamics and localization phenomena in Rydberg lattice gases with position disorder, *Phys. Rev. Lett.* **118**, 063606 (2017).

[121] R. J. Valencia-Tortora, N. Pancotti, M. Fleischhauer, H. Bernien, and J. Marino, Rydberg platform for nonergodic chiral quantum dynamics, *Phys. Rev. Lett.* **132**, 223201 (2024).

[122] Y. Wang, J. Wang, A. Panja, X. Wang, and Q.-Y. Liang, Directional transport in Rydberg atom arrays via kinetic constraints and temporal modulation, *Phys. Rev. Res.* **7**, L022035 (2025).

[123] J. N. Bai, F. Yang, D. Yan, W. Li, and X. Q. Shao, Engineering the non-Hermitian SSH model with skin effects in Rydberg atom arrays, [10.5281/zenodo.18356975](https://doi.org/10.5281/zenodo.18356975) (2026).